Daily Variations of Plasma Density in the Solar Streamer Belt

Morgan, Huw

Published in:
Astrophysical Journal

DOI:
10.3847/1538-4357/ac1799

Publication date:
2021

Citation for published version (APA):
Morgan, H. (2021). Daily Variations of Plasma Density in the Solar Streamer Belt. *Astrophysical Journal*, *922*(2), [165]. https://doi.org/10.3847/1538-4357/ac1799

The Astrophysical Journal, 922:165 (16pp), 2021 December 1 https://doi.org/10.3847/1538-4357/ac1799

Daily Variations of Plasma Density in the Solar Streamer Belt

Huw Morgan
Department of Physics, Aberystwyth University, Ceredigion, Cymru, SY23 3BZ, UK; hmorgan@aber.ac.uk
Received 2020 December 3; revised 2021 July 22; accepted 2021 July 23; published 2021 November 29

Abstract

Improved space weather diagnostics depend critically on improving our understanding of the evolution of the slow solar wind in the streamer belts near the Sun. Recent innovations in tomography techniques are opening a new window on this complex environment. In this work, a new time-dependent technique is applied to COR2A/Solar Terrestrial Relations Observatory observations from a period near solar minimum (2018 November 11) for heliocentric distances of 4–8 $R_\odot$. For the first time, we find density variations of large amplitude throughout the quiescent streamer belt, ranging between 50% and 150% of the mean density, on timescales of tens of hours to days. Good agreement is found with Parker Solar Probe measurements at perihelion; thus, the variations revealed by tomography must form a major component of the slow solar wind variability, distinct from coronal mass ejections or smaller transients. A comparison of time series at different heights reveals a consistent time lag, so that changes at 4 $R_\odot$ occur later at increasing height, corresponding to an outward propagation speed of around 100 km s^{-1}. This speed may correspond to either the plasma sound speed or the bulk outflow speed depending on an important question: are the density variations caused by the spatial movement of a narrow streamer belt (moving magnetic field, constant plasma density), or changes in plasma density within a nonmoving streamer belt (rigid magnetic field, variable density), or a combination of both?

Unified Astronomy Thesaurus concepts: Solar coronal streamers (1486); Solar corona (1483); Solar atmosphere (1477); Solar wind (1534); Slow solar wind (1873); Coronagraphic imaging (313); Astronomical methods (1043); Time series analysis (1916)

Supporting material: animation

1. Introduction

The solar corona, within a few solar radii of the Sun, is a complex magnetic plasma environment that has only been observed remotely. Advancing our knowledge of this system is crucial to understanding the connection between the Sun and the solar wind and the evolution of the nascent solar wind, as well as to correctly model the solar wind in interplanetary space. Without this understanding, there remains a large uncertainty in forecasting space weather, even for periods of quiescent solar wind conditions. Furthermore, without improved observational diagnostics of the corona, large-scale simulations of the solar wind lack observational constraints and remain solely dependent on photospheric magnetic field measurements.

The solar corona, even in the absence of coronal mass ejections (CMEs), is host to dynamic events at a large range of temporal and spatial scales. The global structure of the corona evolves with the solar cycle. The large-scale, high-density streamer regions near the equator at solar minimum migrate to and from the poles in the ascending and descending stages of the cycle surrounding solar maximum. The distribution of streamers in latitude appears to follow the distribution of filaments in the low corona, and the change from a purely minimum equatorial configuration to streamers appearing at mid- and polar latitudes seems to occur quite rapidly (Morgan & Habbal 2010). Whether these long-term changes occur incrementally or in a series of more rapid reconfigurations is unknown. At smaller spatial scales, the coronal density structure seems to be highly filamentary, with high-resolution white-light coronagraph (e.g., Thernisien & Howard 2006; Decraemer et al. 2019) and eclipse images (e.g., Druckmüller et al. 2014; Habbal et al. 2014; Alzate et al. 2017) showing evidence of radial striae, with density contrast between bright striae and their background in streamers up to an order of magnitude (Thernisien & Howard 2006). Small-scale temporal changes that are not CMEs include Sheeley blobs (e.g., Sheeley et al. 1997), periodic density structures (Viall et al. 2010; Viall & Vourlidas 2015), very faint fast and slow propagations emerging from low in the corona (Alzate et al. 2021), and small-scale faint inflows (Wang et al. 1999; Sheeley & Wang 2001; DeForest et al. 2014). These small-scale dynamics all possess spatial scales of less than 1 Mm and occur on timescales less than a few hours. Temporal changes in coronal observations occurring at timescales of a day to a few days are difficult to interpret directly from observation since any observed changes can be due to structures rotating in and out of the line of sight owing to the solar rotation or to true structural or density changes. Separating these two components requires resolving the line of sight.

The properties of the optically thin corona are derived from emissions integrated along extended lines of sight. Interpretations of routine broadband observations made in visible light by coronagraphs, over several decades, are severely limited owing to the line-of-sight problem. Accurate calibration is central to achieving reliable estimates of the electron density. A comprehensive description of coronagraph pre-processing and calibration routines is given by Morgan (2015, hereafter Paper I), and the procedures include an improved radiometric calibration based on observations of stars with an estimated uncertainty of 10%, a detailed cross-calibration between coronagraphs, and a method to separate the F-coronal brightness. Morgan (2019, hereafter Paper II) presents a recent advancement in coronal rotational

tomography that gives maps of the coronal electron density at heliocentric distances greater than $\approx 3\,R_\odot$, at all periods of the solar cycle. The reconstructions are shown to be robust to noise levels of 5% and to data gaps of up to four missing days per 14 days. This approach is a solution that opens a new window on the large-scale density structure of the corona, with initial results and further method developments presented in Morgan & Cook (2020, hereafter Paper III). More details of coronal rotational tomography and past results are given in Paper II and Paper III.

The most common approach to coronal rotational tomography is to assume a static density structure. Two weeks of input observations are required for a tomography reconstruction, and a time-independent density solution is found based on the fit to data and other criteria. There are studies that look at the time evolution of the corona over the short term (Morgan 2011b) and long term (Morgan & Habbal 2010; Morgan 2011a; Morgan & Taroyan 2017) but are based on a series of "snapshots," or static reconstructions, rather than an intrinsic time-dependent approach. Vibert et al. (2016) present a regularized inversion method to find the volumetric time-dependent coronal electron density, and the results of this method are applied to the Large Angle and Spectrometric Coronagraph (LASCO; Brueckner et al. 1995) C2 instrument aboard the Solar and Heliospheric Observatory (SOHO; Domingo et al. 1995) for a data set spanning several years (available at the LASCO-C2 Legacy Archive; see Acknowledgments).

In this work, Section 2 extends the method of Papers I, II, and III to allow a tomography density reconstruction to change over time. Results are presented in Section 3, followed by a discussion (Section 4) and conclusions (Section 5). Further details of the method are given in Appendix A, and a demonstration of the method's convergence is given in Appendix B.

2. Method

The method begins with a static tomographical reconstruction as an initial estimate and uses the residuals between the observed and tomographical coronal brightness to initialize a time-dependent density reconstruction. The method then iteratively improves on this estimate and converges to a solution. In observations, the largest brightness time variations are restricted to the streamer belt, and this is the region where static tomographical reconstructions are most inaccurate. The time-dependent method therefore restricts time variations to the high-density streamer regions. Thus, the positions of the streamers in the static reconstruction are used as a fixed spatial constraint, and density is constrained to vary over time only within the regions defined as streamers. The process iteratively decreases the residuals between reconstruction and observation and smooths the spatial and temporal variations in density at each iteration to avoid abrupt discontinuities that may be unphysical.

The COR2 coronagraphs are part of the Sun Earth Connection Coronal and Heliospheric Investigation (SECCHI; Howard et al. 2002) suite of instruments aboard the twin Solar Terrestrial Relations Observatory (STEREO A and B; Kaiser 2005). Density maps are calculated from COR2A data in three main steps:

1. Calibration is applied to COR2A polarized brightness (pB) observations over a period of half a Carrington rotation (± 1 week from the required mid-date) using the procedures of Paper I. For this work, the mid-date is 2018 November 11 12:00, and the data span a period from 2018 November 04 00:00 to 2018 November 17 23:08. The calibrated input data for a height of $4\,R_\odot$ are shown in Figure 1(a). The cadence of the input data is approximately hourly, with 323 observations spanning the period. The processing steps include decreasing the signal from CMEs using the Dynamic Separation Technique (see Section 3 of Paper I) and the application of correction factors to the individual COR2A images taken at different polarization angles (see Section 5 of Paper I). These correction factors give the best agreement between LASCO-C2 and COR2A pB observations during 2007 March, at a time when both spacecraft viewed the Sun from similar viewpoints near Earth. The estimated radiometric calibration uncertainty for LASCO-C2 is approximately 10%. Following the correction factors applied to COR2A, there is a mean absolute fractional difference of 18% between LASCO-C2 and COR2A pB; thus, we estimate the calibration uncertainty of COR2A at 20%. Slices of the pB images at a constant heliocentric distance are extracted and stacked over time to create a position angle–time observation space. For example, for a reconstruction at a distance of $4\,R_\odot$, the pB profiles are extracted from a thin slice centered at $4\,R_\odot$ in the plane-of-sky image coordinates (see Paper II).
2. Regularized tomography is applied to the data using the spherical harmonic approach of Paper II. In this method, full consideration is given to the true coordinates of the observation in relation to heliocentric Carrington coordinates, including nonparallel diverging lines of sight (small detector, large Sun) and tilt of the solar rotational axis. This method assumes that the coronal density structure is radial and that the density decreases as $r^{-2.2}$ with increasing distances above the reconstruction distance. These two assumptions allow the reconstruction space to be of dimensions longitude and latitude, without the radial dimension, and the reconstruction is made on a spherical shell at a given distance from the Sun. Typically, for a given date, several such reconstructions are made at several distances from the Sun, with each density distribution reconstructed independently of the others. The density distribution, on the sphere, is modeled by a set of spherical harmonic coefficients that are found through the regularized inversion scheme described in Paper II. A 25th-order spherical harmonic basis results in density reconstructions with 540 longitude and 270 latitude bins for a set of nine heights between 4 and $8\,R_\odot$, at $0.5\,R_\odot$ increments.
3. High-density streamers are narrowed, and the correction for "excess" density (possibly F-corona contamination; Morgan & Habbal 2007c) is applied according to the method of Paper III. The streamer narrowing is achieved through applying a spatial narrowing process, with the degree of narrowing controlled by a single parameter. The narrowing process is necessary since we found in Paper II and Paper III that reconstructed streamers were too wide compared to the structures seen in data—probably due to the smoothing effect of the regularization during inversion. Several trial values of the narrowing parameter are applied, and the resulting density for each trial value is adjusted to best fit the data using iterative algebraic reconstruction. The final selection of the optimal narrowing parameter is based on

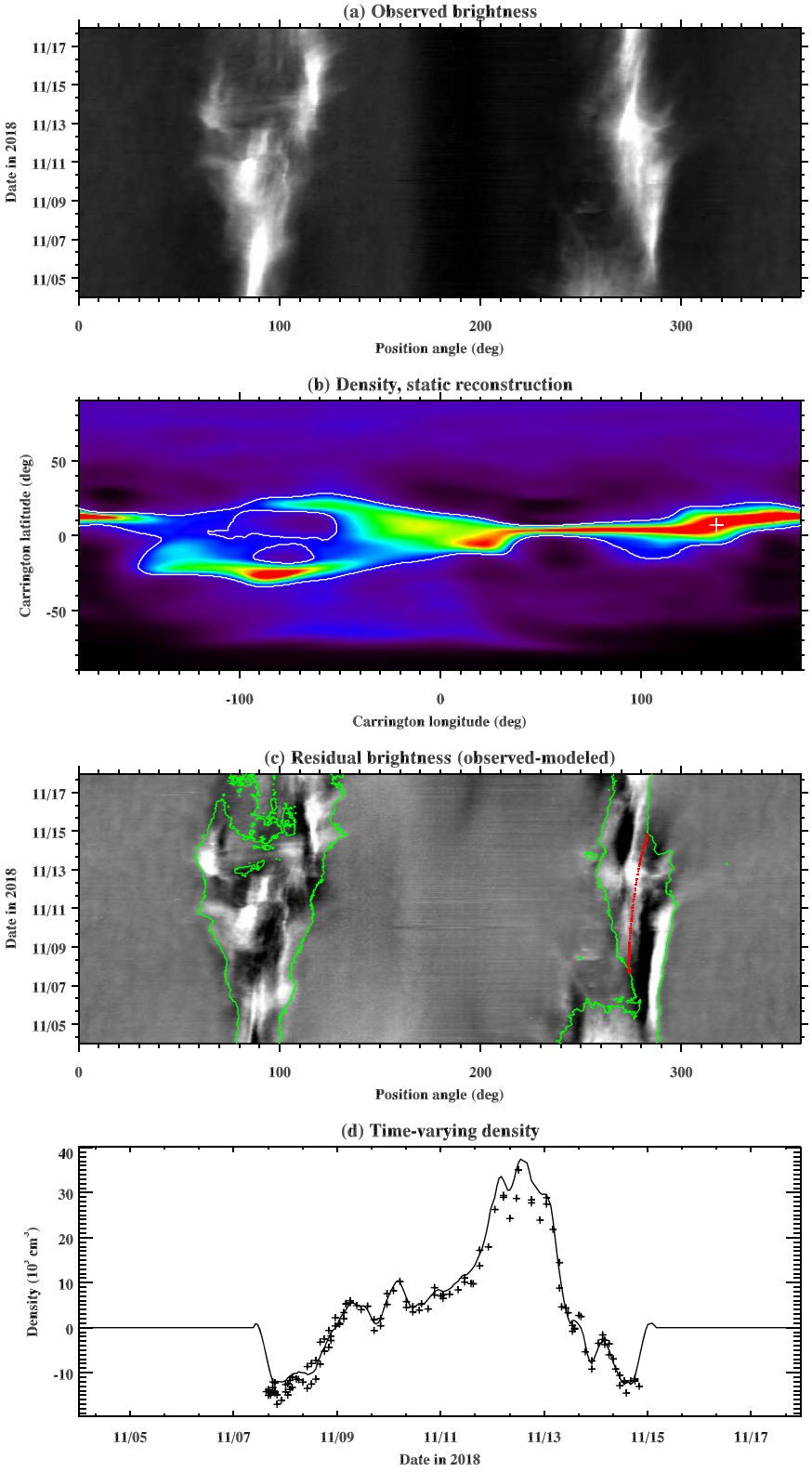

Figure 1. (a) Polarized brightness as a function of position angle and observation time at a height of 4 $R_\odot$ for COR2A observations. Position angle is measured counterclockwise from north. Note that these data are the same as those shown in Figure 1(a) of Paper III. (b) Tomography reconstruction as given by the methods of Paper II and Paper III. Note that this reconstruction is the same as that shown in Figure 6(a) of Paper III. The white contour shows the boundary of streamer regions as defined in the text. The white cross shows a longitude–latitude bin used for describing the method. (c) The residual brightness, given by the observed brightness minus the brightness of the tomography reconstructed corona. The green contours bound areas defined as streamers, and the red points show points in the observed space that are influenced by the density within the longitude–latitude bin shown by a white cross in panel (b). (d) The variation over time of the density in the longitude–latitude bin denoted by the white cross in panel (b), as given by the residual brightness at the red points in panel (c). The crosses show the direct time changes gained from the brightness residuals, and the solid line after the application of a Savitzky–Golay smoothing filter. This filtered time variation is added to the original static density (see text), resulting in a time-varying density reconstruction.

the best structural correlation with the input data. The "excess density" is found through an application of mass flux conservation to density at multiple heights in the lowest-density coronal holes. For this correction, we assume that the fast wind in these coronal holes must maintain a constant speed or accelerate, leading to a corrective subtraction of density with increasing height (hence the term "excess density"; see Paper III).

The resulting tomography density map, as shown in Figure 1(b), shows the distribution of electron density that best satisfies the two weeks of input data given the constraints described in Paper II. In this work, this is called the "static reconstruction," since it has no time dependence. This section gives a general overview of the method for gaining time-dependent density reconstructions, while Appendix A gives a more detailed description.

From the initial static reconstruction, synthetic polarized brightness is calculated through line-of-sight integrations and subtracted from the observed brightness. This residual is shown in Figure 1(c). Black (white) areas are where the synthetic brightness is fainter (brighter) than the observation. In the density reconstruction, areas containing streamers are defined as areas where the density is greater than 1.35 times the mean density and are bounded with a white contour in Figure 1(b). Low-density regions outside this boundary are left unchanged throughout the method. Similarly, within the observation space, regions where the brightness is greater than 1.2 times the mean brightness are defined as streamers and are bounded by a green contour in Figure 1(c). Regions outside of streamers do not influence the calculation of time-varying density. Thus, the high variability of density/brightness within streamers can be explored without contaminating the low-density regions of coronal holes. As shown in Paper III, the density reconstructions give brightnesses that fit the observed coronal hole brightness very closely. It is the bright, high-density streamers that are less well fitted, and in calculating a time-dependent density reconstruction it is important to leave the low-density, faint regions unchanged. The large residual within streamers seen in Figure 1(c) is largely due to the static tomography's inability to address temporal variations. The choice of 1.35 times the mean density to define streamers is based on trial and error, as well as a visual examination of the boundary contours overlaid on the density map. The gradients between streamers and surrounding regions are steep; thus, we have reasonable confidence in this threshold value. At a smaller value (1.3 times the mean density), small regions within the polar coronal holes wrongly become defined as streamers. At larger values (1.4 times the mean density), regions that are obviously part of the continuous streamer belt are excluded. A similar approach is used to define the brightness threshold, which also has steep gradients and thus an obvious delineation between regions strongly influenced by streamers or otherwise. Studies of other periods may require adjustment of these thresholds.

In the density reconstruction, each longitude–latitude point within the streamer belt maps to a set of position angle–time points in the observation space—these are the observed points that are influenced by that reconstruction bin. For illustration, a reconstruction bin is shown by a white cross in Figure 1(b), and the observation points (within streamers) that map to this bin are shown as the red points in Figure 1(c). This path traces the changing position angle, due to solar rotation over time, of the intersection of the observation made at $4\,R_\odot$ and a coronal radial line at the longitude–latitude position. This point varies in heliocentric distance over time, as shown in Figure 2(a). Similarly, the distance of this point along the observer's line of sight is shown in Figure 2(b), measured relative to the point of closest approach to the Sun. Although the heliocentric distance changes over time, we assume that the density structure remains similar over distance (the reconstruction is limited only to a spherical shell at $4\,R_\odot$), and we assume a density decrease of $r^{-2.2}$ for all distances larger than $4\,R_\odot$. Note that the line of sight is curtailed to a maximum range of $2.5r_0$, where r_0 is the heliocentric distance of the point along the line of sight closest to the Sun. For reconstructions made at $4\,R_\odot$, the line-of-sight range is $\pm 10\,R_\odot$ from the point of closest approach to the Sun. The range shown in Figure 2(b) is less than this since, for the selected longitude–latitude point, the range is restricted to the regions within streamers in observation space.

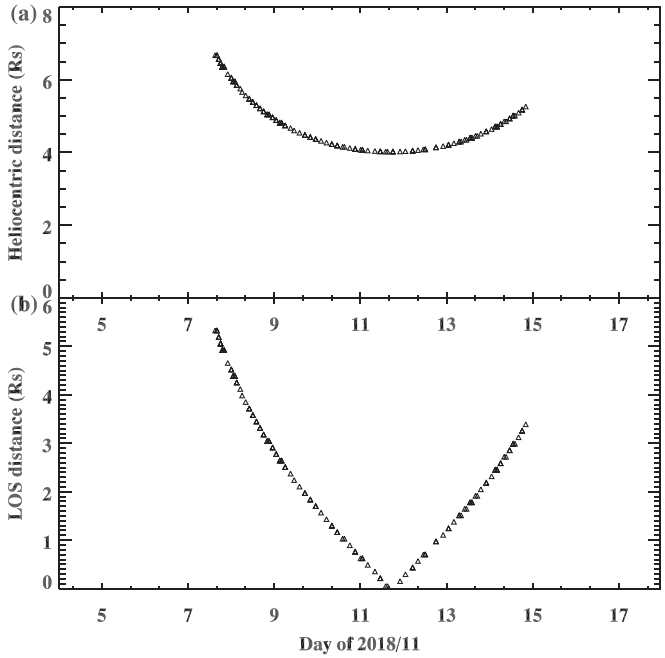

Figure 2. (a) The heliocentric distance as a function of time of the longitude–latitude point indicated by the white cross in Figure 1(b), for an observation made at $4\,R_\odot$. (b) The distance along the observer line of sight, measured from the point of closest approach to the Sun, for the longitude–latitude point.

The residual brightness at each of the position angle–time points is used as an initial estimate of the time-varying density for the reconstruction point. In order to give density, the residual brightnesses in units of mean solar brightness are divided by the known constants and geometrical functions that relate the line-of-sight density to polarized brightness (e.g., Quémerais & Lamy 2002). This density is the mean density required, if integrated along an extended line of sight, to give exactly the residual brightness (see Appendix A). This initial estimate is shown as the crosses in Figure 1(d). The time series is filtered using a Savitzky–Golay smoothing filter, giving the solid line in Figure 1(d). Time steps where no information is available (i.e., when the longitude–latitude bin has rotated out of the field of view of the instrument) are set to zero.

The reconstruction space now has dimensions of longitude, latitude, and time. For each time step, the residual density map is convolved in space with a narrow Gaussian kernel of width $1^\circ \times 1^\circ$ in longitude and latitude (1σ width) and added to the initial static reconstruction. For each time step in the observation, the

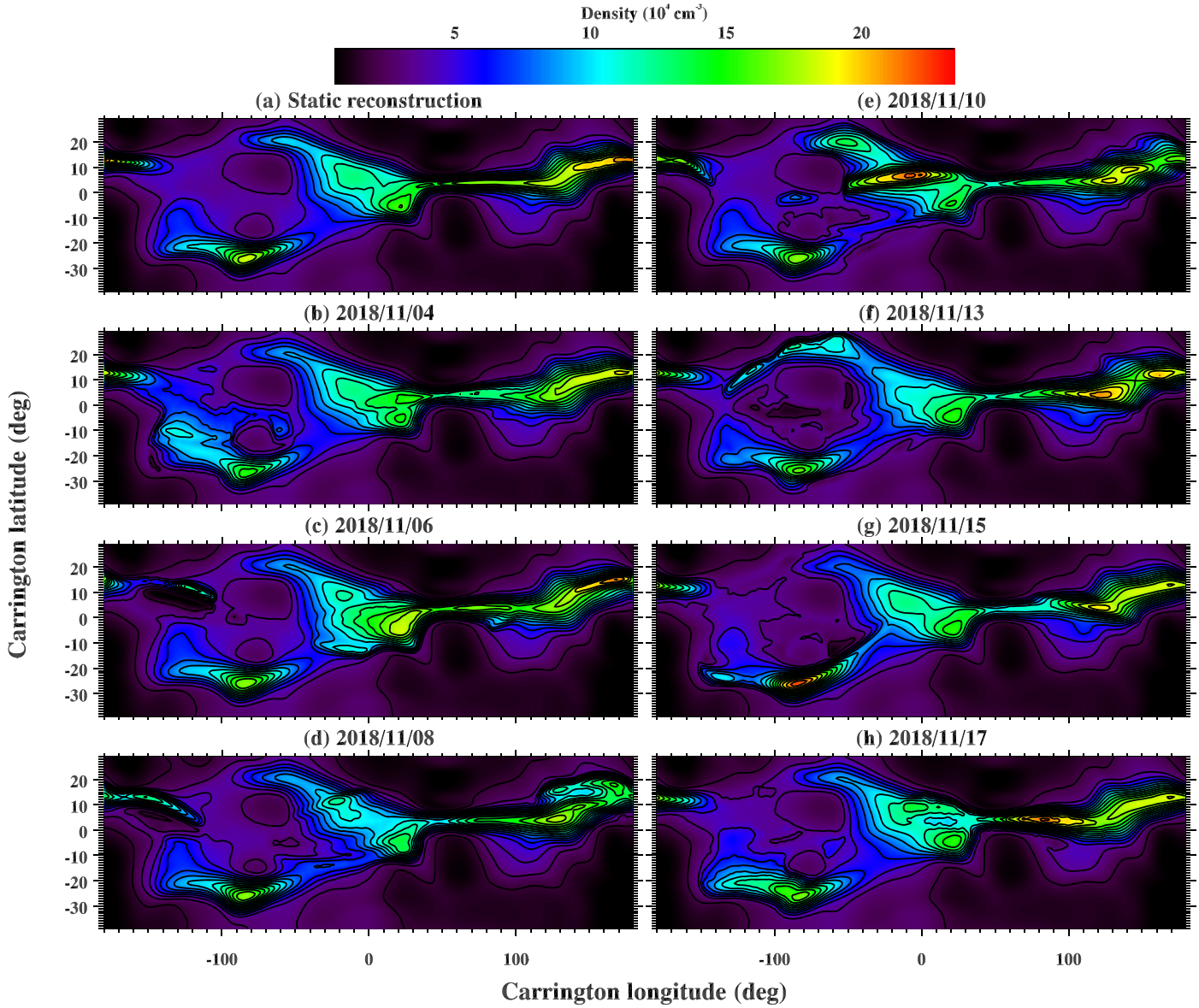

Figure 3. Density of the streamer belt at a height of 4 $R_\odot$ as estimated by (a) the static tomography reconstruction and (b–h) the time-varying reconstruction for the dates indicated in the plot titles. The color bar indicates the electron density in units of 10^4 cm^{-3}. An animation of this figure is available in the online Journal. The animation shows the density evolution at two heights for comparison, 4 (top) and 6 $R_\odot$ (bottom), and it has two chapters. The first chapter shows the time-varying reconstruction from 2018 November 04 00:08 UT through 2018 November 17 22:08 UT. The second chapter of the animation shows the same density minus the static reconstructed density, thus showing more clearly the time evolution of the reconstruction.

(An animation of this figure is available.)

corresponding density map is used to create synthetic observations, and a new set of residual brightnesses are calculated. The process is then iterated until convergence is reached, defined as when the difference between the current and previous iteration's mean absolute residual drops below a small threshold. This iterative process, with forward and backward calculations of density and brightnesses based on the model residuals, has similarities to tomographical algebraic reconstruction techniques. Appendix B shows further details on the convergence of the method for the 2018 November data set.

Note that the time dependency of the density reconstruction adds a new degree of freedom that will, given an appropriate converging method, always result in a closer fit to the data. At each iteration, any regions of the reconstruction space that contain density lower than a certain threshold are set to that threshold. This is calculated as the 10th percentile minimum of coronal hole densities. This is similar to the positive constraint often imposed on solar rotational tomography. The temporal smoothness of the reconstruction is given by the Savitzky–Golay filter over time, and spatial smoothness by the Gaussian smoothing of the residual. The result is a time-varying density, which varies smoothly in time and space and fits the observations closely.

3. Results

Figure 3 shows the application of the method to the COR2A observations of mid-date 2018 November 11 and a height of 4 $R_\odot$. For the sake of comparison, the static reconstruction is shown in Figure 3(a), while Figures 3(b)–(h) show the time-varying density at ≈2-day increments. A movie accompanies this figure, showing in more detail the evolution of the streamer belt density over time. In the movie, the density evolution is

shown at two heights for comparison: 4 (top) and 6 $R_\odot$ (bottom). The movie continues to show, based on the same data, the time-dependent densities minus the static reconstruction, thus showing more clearly the estimated time evolution arising from the method. We emphasize that the time-dependent reconstructions are obtained independently at each height, as are the initial static reconstructions.

There is an apparent continuous drift of density structures within the streamer belt toward decreasing longitude. At any given time, a region of the reconstruction remains constant over time owing to missing observational information, and this region of static density drifts to lower longitudes according to the Carrington rotation rate on which the tomography is based. The regions where observational information is available, where there are time variations in density, also drift in longitude. This leads to the impression of a continuous longitudinal drift of density structure, which is an unavoidable artifact of the method based on observational limitations.

Figure 4(a) shows the observed brightness as a function of position angle and time (same as Figure 1(a)). Figure 4(b) shows the reconstructed brightness for the time-varying reconstruction, while Figure 4(c) shows the reconstructed brightness for the static reconstruction. The mean absolute relative deviation of residuals is 15% for the static reconstruction and 7% for the time-varying reconstruction. In general, the residuals are halved when the density is allowed to vary in time. The mean absolute relative deviation within streamer regions improves from 20% to 3% between the static and time-varying reconstruction (see Appendix B). This improved fit is obvious to the eye from Figure 4. Even fine-scale details of the observed streamer belt, which are often faint, complex, and intricate, are well replicated by the smoothly changing density reconstruction. This is an important result: smooth time variations in density can lead to intricate fine-scale structure in the coronagraph images. This is due to the superposition of structures along an extended line of sight, changing over time. To emphasize this point, Figure 4(d) shows the reconstructed brightness for a static density distribution based on one time slice of the time-dependent reconstruction. For this example the time-dependent density for 2018 November 10 21:08 is used to reconstruct the polarized brightness for all dates. This brightness is different from that of the static reconstruction of Figure 4(c) and retains the same overly smooth distribution. It does not contain the fine-scale structures of the time-dependent reconstructed brightness, thus supporting the assertion that a major component of the fine-scale structure seen in observations can be due to relatively slow time variations.

Figure 5 shows a more detailed comparison of the observed, time-varying, and static brightnesses at certain position angles and times. It is obvious that the new degree of freedom included with the time-varying density gives a far closer fit to the data. The static reconstruction fails to fit the high, narrow brightness of the streamer belt (e.g., Figures 5(c) and d), and the position angles of some peaks are incorrect. The time-varying reconstruction very closely fits all major brightness peaks in the streamer belt—in position angle and time. Therefore, the high brightness and intricate narrow structure of streamers in coronagraph images are a result of large density temporal variations. The density variations shown in Figure 3 and the accompanying movie are a smoothed approximation to the true variation.

Figure 6(b) shows changes in density over time for four points along the streamer belt. Density can, over a typical period of 2–4 days, increase by factors of two or three. For

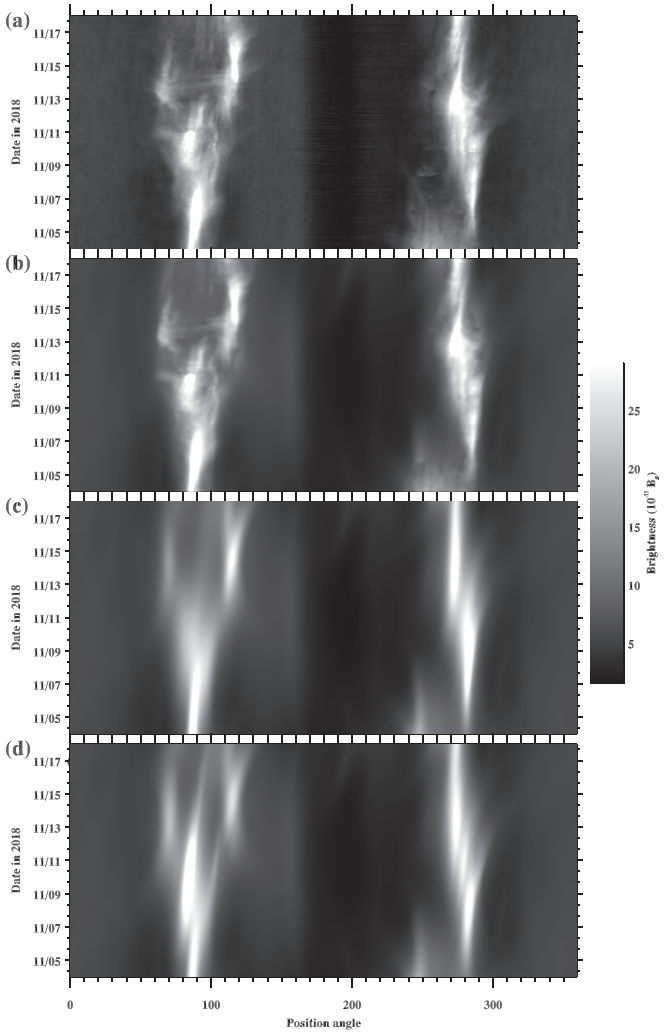

Figure 4. Polarized brightness as a function of position angle and observation time at a height of 4 $R_\odot$ for (a) COR2 observations, (b) the time-varying tomography reconstruction, (c) the static tomography reconstruction, and (d) the brightness arising from using one time step of the time-varying tomography reconstruction (at 2018 November 10 21:08) as a static reconstruction (see text). The color bar indicates the polarized brightness in mean solar brightness units of 10^{-11} $B_\odot$. Position angle is measured counterclockwise from north.

the static reconstruction at 4 $R_\odot$, the mean streamer belt density is 10^5 cm^{-3}, with a range of (0.5–1.8) $\times$ 10^5 cm^{-3}. Previous nontomographical inversion studies at 4 $R_\odot$ give streamer belt densities of 1.3 $\times$ 10^5 cm^{-3} (Gibson et al. 1999), 1.4 $\times$ 10^5 cm^{-3} (Morgan & Habbal 2007c), 1.8 $\times$ 10^5 cm^{-3} (Hayes et al. 2001), and 2.2 $\times$ 10^5 cm^{-3} (Strachan et al. 2002). A time-dependent tomographical reconstruction for 2016 October, based on LASCO-C2 data and accessed via the LASCO-C2 Legacy Archive (see Acknowledgments), gives streamer belt densities in the range of approximately (1–2) $\times$ 10^5 cm^{-3} (Vibert et al. 2016). Figure 6(b) shows that the time-varying density can, at certain positions and periods, reach high densities at around twice the mean density and exceed the high estimate of Strachan et al. (2002). These peaks have a duration of a day or a few days. Some regions of the streamer belt can experience significant dips in density lasting a few days. One example is the brown line of Figure 6, where the density decreases over 2 days to a minimum of around half the mean density at 2020 November 15 00:00UT, before increasing over the course of another 3 days.

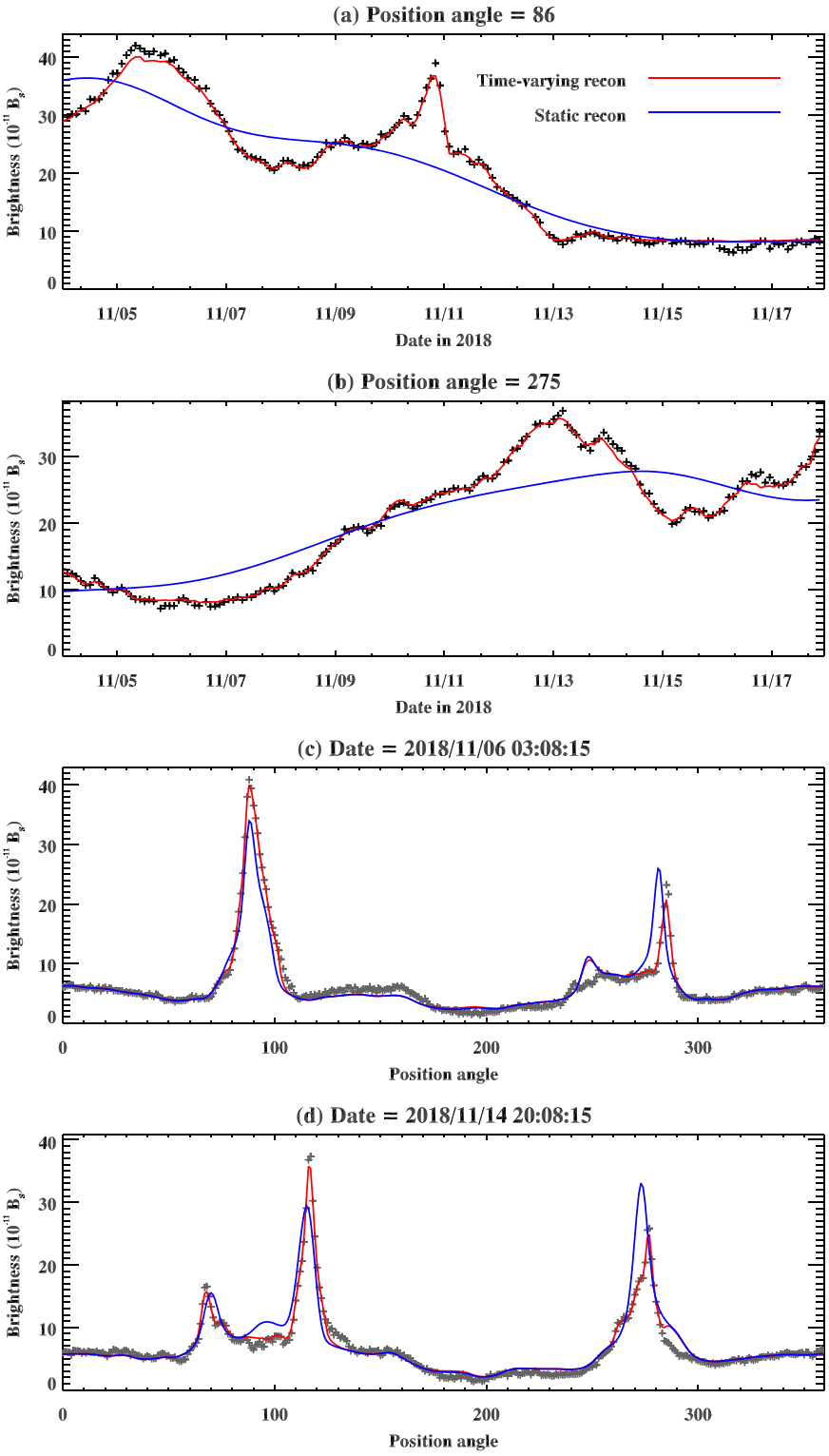

Figure 5. Profiles of polarized brightness vs. time at position angles centered on the (a) 86° east streamer belt and (b) 275° west streamer belt, and versus position angle at dates (c) 2018 November 06 03:08 and (d) 2018 November 14 20:08. The black crosses show the COR2A observation, the blue lines show the static reconstruction, and the red lines show the time-varying reconstruction.

3.1. Comparison to In Situ Measurements

During 2018 November the Parker Solar Probe (PSP) was at perihelion. The path of PSP is extrapolated downward to a height of 8 $R_\odot$ using the known spacecraft position and the measured radial proton velocities. This extrapolated path is shown in the context of the coronal density in Figure 7(a) and is labeled with letter S for start (2018 November 06 00:00) and E for end (2018 November 17 00:00). For a given measurement by PSP, the measured proton radial velocity and spacecraft radial distance are used to calculate the time of travel from 8 $R_\odot$ assuming a constant speed. Assuming a Carrington rotation rate to the corona, the travel time equates to a

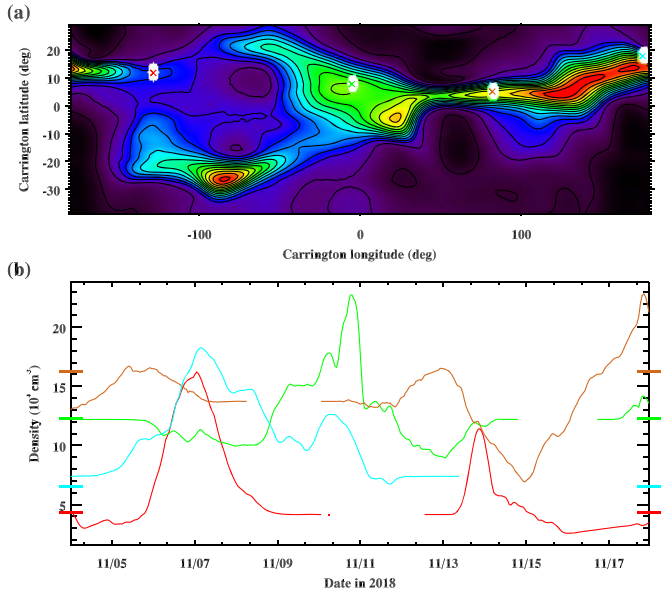

Figure 6. Examples of the time variation of density within the streamer belt. (a) Density map at a height of $4\,R_\odot$ (density averaged over time), showing the streamer belt, and four selected points shown with colored crosses. Four points showing large density variation have been selected. (b) Density vs. time for the four selected points. Times when that region of the corona is not observed, and therefore no information is available on the density time evolution, are treated as missing data and result in gaps in the time profiles. The short horizontal colored bars cutting across both *y*-axes show the value of density at each point for the static tomography reconstruction.

longitudinal shift; thus, the coordinates of PSP over time are mapped to a set of coordinates on the tomographical map.

The Solar Wind Electrons Alphas and Protons (SWEAP) instrument on PSP samples proton velocity distributions. The proton density, averaged over 1 hr periods between November 6 and 16 and normalized to the perihelion height of $36\,R_\odot$ using a mass flux constraint for spherical expansion, is shown in Figure 7(b). This direct measurement provides a valuable comparison to the time-varying tomographic coronal density. This comparison is based on the assumption that the streamer belt magnetic field at distances of $8\,R_\odot$ and greater is open. While the streamer belt overlies large-scale closed field structures near the Sun, and the bulk of high-density slow flows are thought to arise from open fields bounding these closed structures (e.g., Abbo et al. 2016), the assumption of open field at heights of approximately $3\,R_\odot$ and larger is reasonable, although there is evidence of expanding closed structures joining the slow wind at extended distances in certain regions above active regions containing emerging flux (Morgan 2013; Morgan et al. 2013). This is not apparent in the 2018 November data set. We note also that equatorial coronal holes can also host slow solar wind flows, as is apparent from recent PSP results (Bale et al. 2019).

Figure 7(c) shows the corresponding tomographical coronal densities along the PSP path at a height of $8\,R_\odot$. The blue line shows the static reconstruction, the black line the time-varying reconstruction. To the eye, it is clear that the time-varying density is in better general correlation with the PSP measurements compared to the static reconstruction. Between 2018 November 06 and 10 PSP measures a general decrease in density, reaching a minimum at around 2018 November 09 18:00UT. The density subsequently increases to a maximum on 2018 November 13. A similar general profile is estimated by the tomography, albeit with less variation on the daily scale. A local minimum is estimated at around 2018 November 09 18:00UT, with a small decrease and increase over the same periods as measured by PSP. The maximum coronal density is estimated to occur early on 2018 November 13, within a few hours of the maximum measured by PSP. Following this, there is a sharp drop to low density, seen in the tomography estimates and by PSP. The tomographical density at $4\,R_\odot$, shown in Figure 7(e), has a more pronounced density decrease and increase during the first 7 days, compared to that of $8\,R_\odot$, and seems in better agreement with PSP.

The correlation between the tomography and PSP densities is 61%. PSP measures a far higher hourly variation in density compared to the tomography. Over the 11-day period, the ratio of the standard deviation to the mean is 56% for the PSP measurements and only 28% for the tomography. It is also clear that the PSP density starts with a fluctuating decrease to a low value, has a broad peak from November 11 to 15, and decreases to low levels, whereas the tomography also shows a general decrease in the first few days, but from a considerably relatively higher value, compared to the maximum density. Thus, the broad peak seen by PSP is less pronounced in the tomographical density. We note that the PSP density measurements are made over a large range of heights and that the mass flux assumption to extrapolate to a single height ($36\,R_\odot$) introduces a large uncertainty.

3.2. Comparison of Time Variation at Different Heights

Figure 8 shows, for three selected points within the streamer belt, density time variations at nine heights between 4 and $8\,R_\odot$. To aid comparison, the density profiles are scaled between heights. There is a clear and consistent lag in time variation between 4 and $8\,R_\odot$. Variations at lower heights are replicated at larger heights a few hours later. This lag is apparent for most significant time variations throughout the streamer belt, but it is sometimes not present, as is the case for the start of the broad day-long peak seen at 2018 November 07 in Figure 8(c). In this case, the clear peak at $4\,R_\odot$ seems to broaden and develop a double peak at larger distances. The movie accompanying Figure 3 shows changing density at 4 and $6\,R_\odot$, and the time delay between heights is apparent to the eye from a careful viewing.

Comparing the profiles at different heights gives a general outward propagation speed of approximately $100\,\mathrm{km\,s^{-1}}$ to the time variations. One example, with a speed of $124\,\mathrm{km\,s^{-1}}$, is illustrated in Figure 8(a). The density variations are not CMEs or transients. The streamer belt density varies over hours or days, and these variations span spatial scales of 10 or tens of degrees in longitude. The changes occur at lower heights, propagating outward at around $100\,\mathrm{km\,s^{-1}}$, possibly linked to the outflow speed of the slow solar wind at these heights (see Paper III, and references within). Another possibility is the coronal sound speed, which is $118\,\mathrm{km\,s^{-1}}$ for a 1.0 MK isothermal plasma. This is discussed further in Section 4.

3.3. Statistical Aspects

Figures 9 and 10 show certain statistical aspects of the density time variation at a height of $4\,R_\odot$. Figure 9(b) shows the standard deviation of variation over time, and Figure 9(c) shows the standard deviation relative to the mean density, with Figure 10(a) showing the corresponding histogram. Some regions show close to zero time variation, while the most

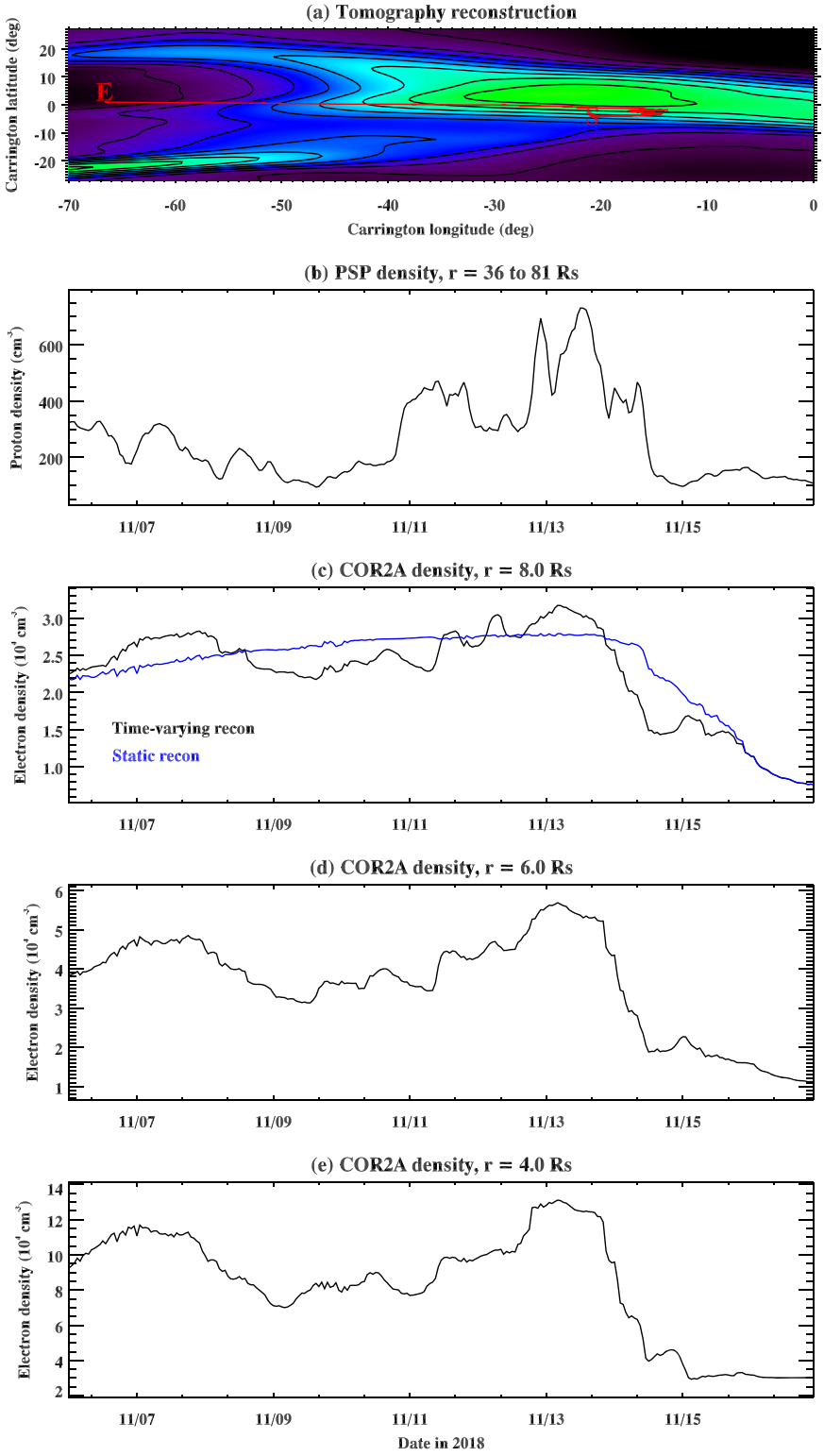

Figure 7. (a) Part of the tomography density map at a height of 8 $R_{\odot}$, showing the path of PSP during perihelion between dates 2018 November 06 and 17 in red. This path has been ballistically extrapolated from the position of PSP, and the bulk radial outflow speed of protons measured by PSP. The start of the path is labeled S, the end with E. (b) The proton density measured by PSP for the 11-day period, averaged over 1 hr periods, and normalized to the closest perihelion height of 36 $R_{\odot}$ (see text). (c) The tomographical time-dependent density along the extrapolated path of PSP at 8 $R_{\odot}$ is shown with the black line. The blue line shows the density for the static reconstruction. (d, e) Same as panel (c), but at heights of 6 and 4 $R_{\odot}$, respectively.

probable variation is around 15% of the mean density. The highest standard deviations are up to 60% of the mean density. Figure 9(b) shows bands of high variation aligned longitudinally across the streamer belt. The variation relative to the mean (Figure 9(c)) shows highest values near the streamer belt boundaries—this is due to the lower mean density in these regions. There is increased time variation near the splitting of the streamer belt between $-20°$ and $-160°$ longitude,

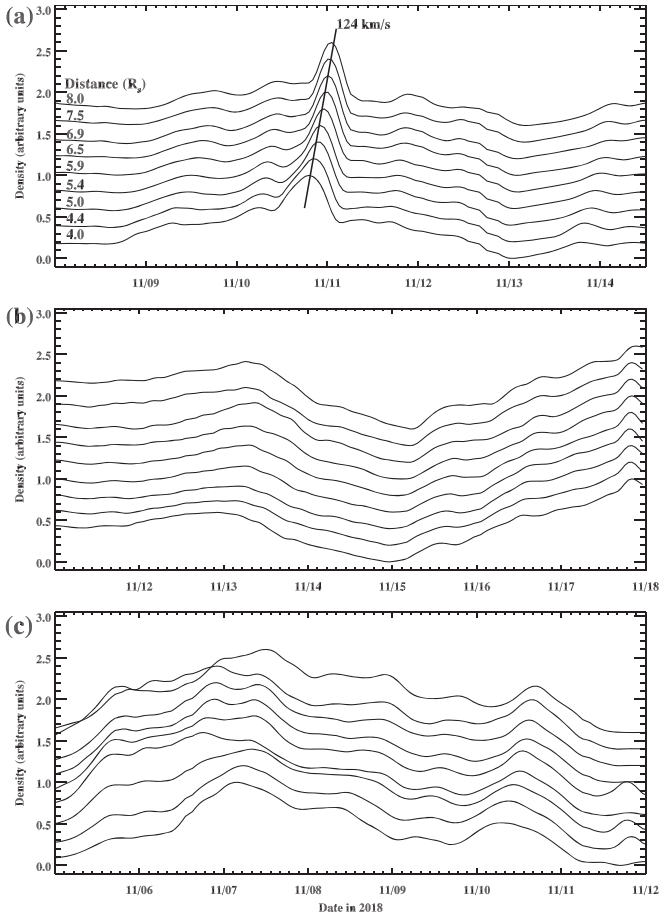

Figure 8. Density variations over periods of several days at nine heights between 4 and 8 $R_\odot$ for Carrington longitude, latitude (a) −44°, 1°, (b) 77°, 4°, and (c) 175°, 16°. The density units are arbitrary: profiles are scaled and stacked in order to compare the variation at different heights. The top panel includes a straight line corresponding to an outward radial speed of 124 km s^{-1}.

suggesting that such streamer−pseudostreamer splittings may be the regions of greatest time variation.

Maximum densities over time are shown in Figure 9(d), with the corresponding histogram of maximum densities relative to the mean densities in Figure 10(b). Broad regions of the streamer belt, particularly near the central current sheet (i.e., at the central position of the streamer, and the south branch of the streamer splitting at negative longitudes), record maximum densities of around 2.3×10^5 cm^{-3}. The most probable maximum density relative to the mean density is 1.3, with the bulk of points proving maxima that are between 1.1 and 1.8 times the mean density. Minimum densities over time are shown in Figure 9(e), with the corresponding histogram of minima relative to the mean in Figure 10(c). Densities can drop as low as 10% of the mean density, with the most probable minimum density relative to the mean being 75%, with the bulk of points proving minima between 50% and 80% of mean density. Figure 10(d) shows the range (maximum minus the minimum) relative to the mean density. For most points, the range is comparable to the mean density, with some points showing a range twice the mean, or higher (mostly distributed at the streamer belt boundaries, where the mean density is low).

4. Discussion

There is no direct independent measurement that can unambiguously quantify the accuracy of time-dependent coronal tomography. The best test currently is to compare with PSP measurements during periods of perihelion. One such comparison, presented in Section 3.1, is encouraging: the general profile of density variation over the course of 11 days is in reasonable agreement. This comparison gives confidence in the time-dependent tomographical approach. While this type of inversion problem can lead to an infinite set of solutions that can exactly match the input data, our results are constrained by smoothness in space and time and are constrained to positive densities. Despite these constraints, our reconstructed brightnesses match the coronagraph data closely. Based on these criteria, and in the absence of PSP comparison, the solutions provided by the time-dependent tomography are valid and credible. One possibility to increase confidence in the results, and to quantify uncertainties, is to compare time-dependent tomographical results between data from different instruments/spacecraft (e.g., LASCO-C2 and COR2A), and using different methods (e.g., Vibert et al. 2016). This is something we hope to do in future work.

Comparing the time-dependent tomography results with PSP depends on a mapping from the PSP position to 8 $R_\odot$, based on the PSP-measured bulk radial proton speed. There are uncertainties associated with this mapping. The slow solar wind is accelerating above 8 $R_\odot$ (see, e.g., Paper III), so the travel time from 8 $R_\odot$ to the PSP position is underestimated, and the calculated longitudinal shifts are also underestimated. For a wind accelerating from 150 to 300 km s^{-1} between 8 and 33 $R_\odot$, this amounts to a 3° underestimate in longitude. Another uncertainty is the coronal rotation rate (see, e.g., Morgan 2011a). Our work on a follow-up study to Morgan (2011a) suggests that the equatorial corona during 2018 is rotating at around 0.°5 day^{-1} faster than Carrington, which again leads to a small underestimation of the longitudinal shift of a fraction of a degree. The approach of assuming a constant solar wind speed and a standard rotation rate is one commonly used in the field (e.g., Badman et al. 2020), and the resulting underestimations of longitudinal shift amount to the order of 5° at most. Another critical question is whether the nature of the solar wind changes significantly between 8 $R_\odot$ and the position of PSP during the 2018 November perihelion (≈30 $R_\odot$ and larger; DeForest et al. 2016, 2018). Such changes may be expected at small spatiotemporal scales, but our comparison looks toward the larger scales of several hours and days. We expect the density structure at these large temporal (and spatial) scales to correlate reasonably between 8 $R_\odot$ and the perihelion distances of PSP, particularly since the predominant magnetic field configuration is radial at these distances. We note that the comparison we make is similar in essence to comparisons made of the magnetic field measured by PSP and of coronal magnetic models (e.g., Bale et al. 2019; Badman et al. 2020): such comparisons are only currently meaningful across broad spatiotemporal scales and cannot yet be applied to small scales. This is due to the uncertainties in the coronal model or reconstruction and the uncertainties associated with the ballistic extrapolation method.

The comparison with PSP suggests that the tomography may oversmooth the reconstructed density variations: the variations measured by PSP vary more on a daily basis than the tomography. Either this or the solar wind somehow amplifies density variations with increasing distance in the extended

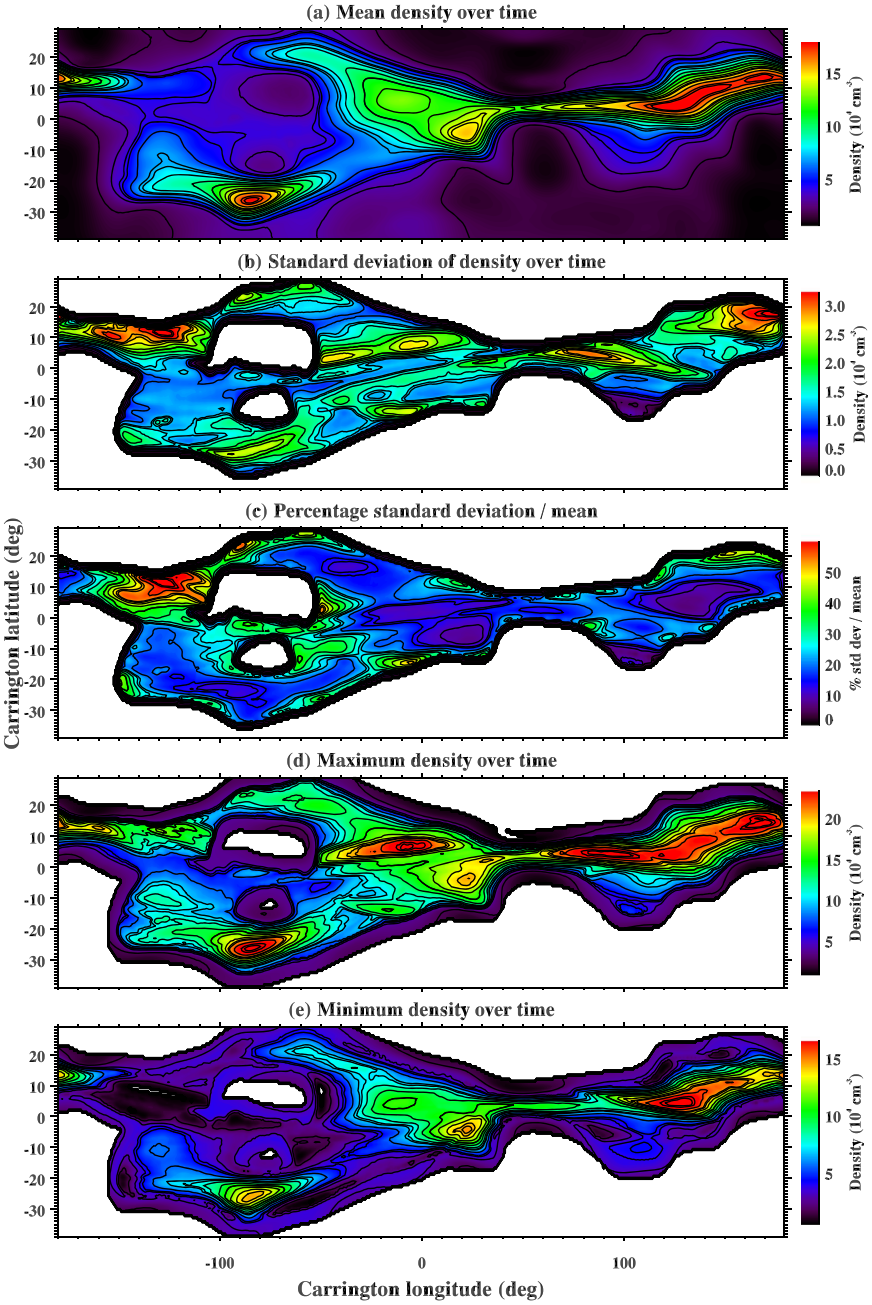

Figure 9. (a) The mean density in the streamer belt over time for a height of 4 $R_\odot$. (b) The standard deviation of density calculated at each longitude−latitude point over time. (c) The percentage standard deviation density over the mean density. (d) The maximum density value over time. (e) The minimum density value over time.

corona. For each spatial voxel contained within the streamer belt, we calculate the standard deviation of temporal variations and divide by the mean voxel density to gain a relative measure of density variation. This information is presented alongside other statistical values in Section 3.3. Furthermore, for each height investigated, we calculate a mean relative variation across the whole streamer belt. This value starts at 20% at 4 $R_\odot$ and decreases linearly with increasing height to 10% at 8 $R_\odot$. Thus, the temporal variations become less pronounced with distance from the Sun. However, PSP shows greater variation. This suggests that the true spatiotemporal density variations have a larger amplitude than those revealed by the tomography and must consequently have higher spatial and temporal frequencies. During most periods of the solar cycle, the streamer belt or belts are aligned longitudinally at low to midlatitudes along the observational lines of sight. Thus, rapid, localized changes in density are convolved along the line of sight and, given the slow rotation of the Sun on which the tomography is reliant, cannot be fully resolved. Thus, the method presented in this paper probably reveals a smoothed variation compared to the true one.

There are additional sources of error that relate to two of the central underlying assumptions of the method: that the coronal structure is purely radial, and that the density decreases with a uniform dependence with heliocentric distance. Results relating to the static reconstructions (as, e.g., presented in Paper III) show that the coronal structure approximates well to radial at the heights of interest presented here. The choice of density decrease with distance is described with Equation (A2) in Appendix A. We should not expect the density to decrease

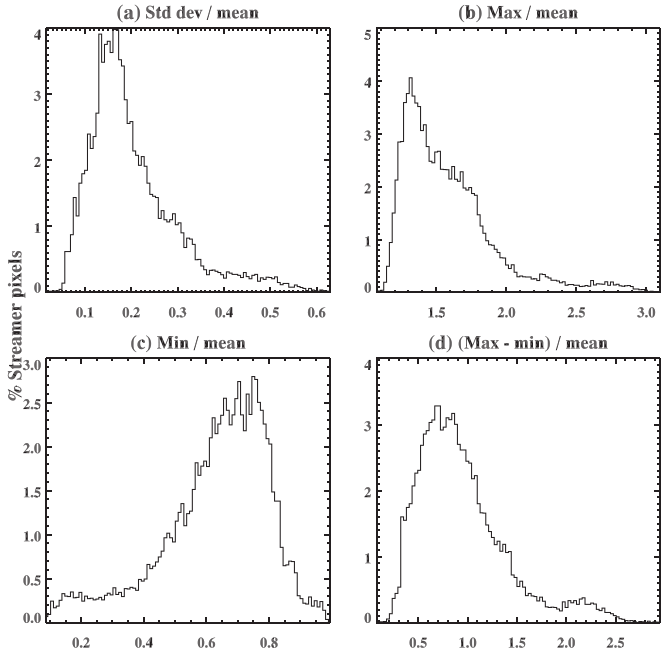

Figure 10. Histograms showing the percentage of all streamer pixels in each bin, for (a) the standard deviation over the mean density over time, (b) the maximum density over the mean density, (c) the minimum density over the mean density, and (d) the density range (maximum minus the minimum) over the mean density.

uniformly in such a way across the corona, for example, given the different acceleration profiles of streamers and coronal holes. Paper II shows, using a reconstruction applied to a simple model density distribution, that the choice of uniform dependence on distance does not impact greatly on the reconstructed densities. More complicated density distributions may have a greater impact. A more advanced method could extract the estimated radial profiles of density from a set of tomography maps spanning a height range and recalculate the tomography reconstructions from the spatially varying height profile given by this information; this is something that may be explored in future work. Another useful future study, at least in the context of method development and validation, would be a detailed comparison with the results of Vibert et al. (2016).

The method is based on defining a region as the streamer belt, and it limits time variations to these regions. This spatial constraint is a model of a static streamer belt, with temporal variations in density constrained to be within the fixed spatial distribution. However, the true corona may contain very narrow, high-density, sheet-like structures (see, e.g., Morgan & Habbal 2007a, 2007b) of constant density that are moving: drifting in latitude or longitude over timescales of tens of hours or days (see also Morgan 2011b). This is a different concept from that of changing plasma density within a quasi-rigid magnetic structure. A moving narrow streamer belt with a time-constant density would show as a temporal variation in density in our method, but the method does not account for these motions. To illustrate, Figure 11 shows the observed polarized brightness at a height of $4\,R_{\odot}$ during 2019 March. This is a striking example of how the streamer belt can change position very rapidly. In late 2019 March 12, there is a large CME. Following this CME, the streamer belt, particularly at the west limb, is severely disrupted. Its position angle is abruptly shifted

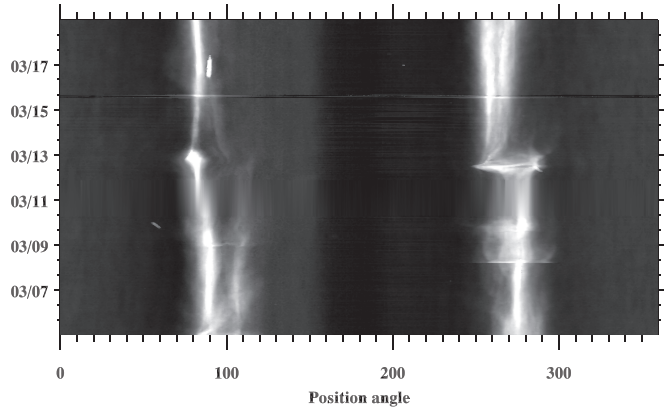

Figure 11. Polarized brightness as a function of position angle and time at a height of $4\,R_{\odot}$ for COR2 observations during March 2019.

southward by 10°–20°. This is a clear example of a rapid change in the magnetic configuration of the streamer belt, and our current method fails to reconstruct using these data. This is an important weakness that is crucial to address in future work. An optimal method would allow the streamer belt distribution to drift in position over time, sometimes rapidly, and also allow variations in density within the belt. We believe this to be entirely possible, but challenging.

Regardless of the two possible interpretations, the time lag of variations with increasing distance from the Sun applies to both and is an exciting result. Large variations in density occur later at increasing distances—changes are imposed lower in the corona and are carried outward at around $100\,\mathrm{km\,s^{-1}}$. This could be linked to the slow solar wind speed at these distances. However, if the density variations are caused by the spatial motion of narrow streamer sheets, this speed could be linked to the coronal sound speed ($118\,\mathrm{km\,s^{-1}}$ for a 1.0 MK isothermal plasma). Thus, a disturbance to the position of streamers low in the corona is propagated outward through the extended corona at the sound speed. The cause of these disturbances needs to be investigated further. Obvious large-scale magnetic reconfigurations can result owing to large eruptions (e.g., Figure 11). We believe that there are also more continuous, gradual streamer motions, possibly associated with large-scale, long-period instabilities or oscillations, or interchange reconnection at streamer boundaries over longer periods. These effects can be investigated with models and simulations constrained by time-dependent coronal tomography. An empirical study would require the advances in coronal tomography described above and connections to be made to observations of the lower corona.

5. Conclusions

Advanced tomography is used to resolve relatively slow density changes in the streamer belt. The streamer belt has a large time-varying density range (maximum minus minimum) of 50%–150% of the mean density. This degree of variation, on timescales of hours or days, is a major component of streamer belt variation that cannot be defined as small-scale transients or CMEs. This study shows that rotation of a static density distribution cannot lead to the observed variations; rather, the streamer belt must be experiencing temporal changes. We believe that the amplitude of the density variations must form a

major component of slow solar wind variability, at least on timescales of tens of hours to days.

From this study, an important question is raised: are the density variations caused by the movement of a narrow streamer belt, or changes in density within a nonmoving streamer belt, or both? Addressing this question has large implications for understanding the corona, for interpreting other types of observations, and for the development of accurate solar wind models. The critical demand of increased space weather forecast accuracy cannot be achieved without a deeper understanding of streamer belt, and thus slow solar wind, variability. Coronal tomography will play a major role in this effort.

We acknowledge (1) STFC grants ST/S000518/1 and ST/V00235X/1, (2) Leverhulme grant RPG-2019-361, (3) the excellent facilities and support of SuperComputing Wales, and (4) the NASA PSP Mission and SWEAP team led by J. Kasper for use of data. The STEREO/SECCHI project is an international consortium of the Naval Research Laboratory (USA), Lockheed Martin Solar and Astrophysics Lab (USA), NASA Goddard Space Flight Center (USA), Rutherford Appleton Laboratory (UK), University of Birmingham (UK), Max-Planck-Institut fur¨ Sonnensystemforschung (Germany), Centre Spatial de Liege (Belgium), Institut Optique Théorique et Appliqúee (France), and Institut d'Astrophysique Spatiale (France). This work makes use of the LASCO-C2 legacy archive data produced by the LASCO-C2 team at the Laboratoire d'Astrophysique de Marseille and the Laboratoire Atmosphères, Milieux, Observations Spatiales, both funded by the Centre National d'Etudes Spatiales (CNES). LASCO was built by a consortium of the Naval Research Laboratory, USA, the Laboratoire d'Astrophysique de Marseille (formerly Laboratoire d'Astronomie Spatiale), France, the Max-Planck-Institut für Sonnensystemforschung (formerly Max Planck Institute für Aeronomie), Germany, and the School of Physics and Astronomy, University of Birmingham, UK. SOHO is a project of international cooperation between ESA and NASA.

Appendix A
Detailed Description of the Method

This appendix gives more detail of the method through the following step-by-step description:

1. A regular longitude−latitude grid of density $\rho(\theta, \phi)$ is initialized as a static tomographical reconstruction at a given heliocentric distance r_0. Typically the longitude, latitude binning is $[2/3°, 2/3°]$; thus, there are 540 longitude and 270 latitude bins. Each bin contains a value of the electron density in units of electrons cm^{-3}.
2. Points in ρ belonging to a streamer are defined as those points that have a density greater than 1.35 times that of the mean density (as shown in Figure 1(b)). These streamer bins are indexed i in the longitude dimension and j in the latitude dimension.
3. The observed polarized brightness, $B(\Omega, T)$, is binned on a regular grid in position angle Ω and time T, at the fixed heliocentric image−plane distance r_0. Typically there are 720 position angle bins and approximately 320 time bins spanning a half solar rotation ($\approx$ 14-day) period. For the case shown of the 2018 November data set there are 323 time steps, and the cadence is exactly 1 hr, except for nine time steps that are 2 or 3 hr. These "missing" hours are due to errors in the original observations and/or the calibration/processing steps and are subsequently treated as missing data throughout the method. This regular time grid is also used as the time binning of the time-dependent density.
4. Points in B belonging to a streamer are defined as those points that have a brightness greater than 1.2 times that of the mean observed brightness. These observation bins are indexed k in the position angle dimension and t in the time dimension.
5. ρ is rebinned (or repeated) across a time dimension matching that of the observation space, becoming $\rho(\theta, \phi, T)$.
6. A synthetic pB observation B' is calculated through line-of-sight integrations of the density ρ. Thus, for each $B_{k,t}$, a line of sight S is constructed through the corona (extending to a range of $\pm 2.5 r_0$ from the point of closest approach to the Sun along the line of sight), and the following summation is calculated:

$$B'_{k,t} = \sum^{S} g_s f_s \rho(\theta, \phi, t) \Delta s, \tag{A1}$$

where s indexes the regular intervals along S, and Δs is the width of the interval. g_s contains the known constants and geometrical functions that relate the line-of-sight density to polarized brightness (e.g., Quémerais & Lamy 2002). f_s is a function that allows for the assumed drop in density with heliocentric distance, given by

$$f_s = \left(\frac{r_0}{r_s}\right)^{2.2}, \tag{A2}$$

where r_s is the heliocentric distance of the line-of-sight bin s. Note that the calculation of B' is made for the whole of ρ and is not limited to the streamer regions.

To help visualize the mapping from the observation space to the reconstruction space, Figure 12(a) shows how a selected set of points in observation space (selected position

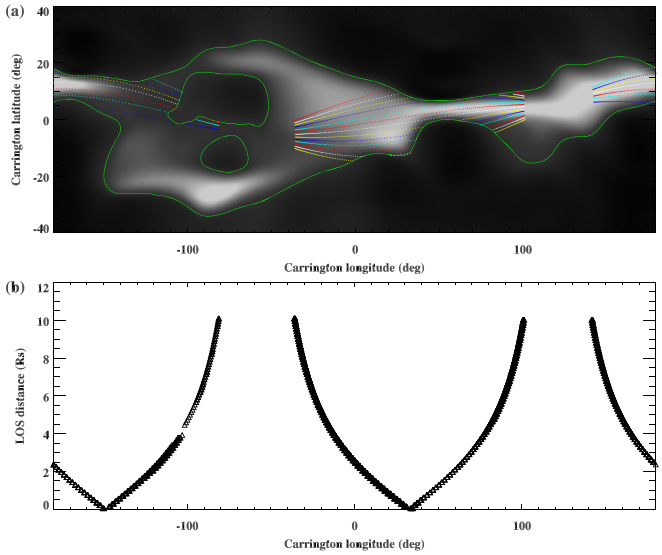

Figure 12. (a) The tomographical density map showing the streamer belt region. Streamers are bounded by the green contour. The arbitrarily colored lines show a set of 20 lines of sight corresponding to 20 selected position angle points, from a single time step, in observation space. The selected time step is for date 2018 November 06 03:08. (b) The distance along the observer line of sight, measured from the point of closest approach to the Sun, for the 20 lines of sight.

angles at a given time step) maps to extended lines of sight in the reconstruction space. Note that these lines of sight are curtailed to only those regions defined as streamers in the reconstruction space. For clarity, only 20 lines of sight are shown here, whereas the total number of position angle points for this time step is 83, giving a dense distribution. The two streamer belt regions that are void of lines are regions that are not observed at that point in time (because the $\pm 10\,R_{\odot}$ range limit on the line of sight does not reach these voids). Progressing through time in observation space will gradually shift these lines and voids to smaller longitudes in reconstruction space (the lines of sight drift from right to left over time). Figure 12(b) shows the distance along each line of sight measured from the point of closest approach to the Sun.

7. Evaluate the residual polarized brightness $R = B - B'$.
8. Each reconstruction streamer bin $[i, j, t]$ is mapped to a point in observation space. Over time, these points describe a path showing where the observation may be influenced by the reconstruction longitude, latitude bin (e.g., the white cross in Figure 1(b) maps to the red points in Figure 1(c)). Note that this path in observation space is curtailed to segments that pass through observation streamer regions. Values are extracted along this path, giving a set of polarized brightness residuals, $R_{k,t}$, that are associated with the reconstruction bin $[i, j]$. $R_{k,t}$ is a function of position angle and time, and its variation in time sets the basis for estimating the density time dependence. For this reason and for clarity, we retain the t index only and discard the k index; thus, $R_t \equiv R_{k,t}$.
9. Each member of R_t is converted into a residual density, P_t, by evaluating the mean density, along extended lines of sight, that would give exactly R_t:

$$P_t = \frac{R_t}{\sum^{S} g_s f_s \Delta s}, \tag{A3}$$

noting that P can be negative (since we are evaluating residual densities).

10. Missing (or unobservable) intervals of P are set to zero. An example is shown in Figure 1(d).
11. P is smoothed over time using a zero-order, third-degree, Savitzky–Golay filter of width 11 time steps.
12. Steps 9−11 are applied to all reconstruction space points $[i, j]$. This results in a time-dependent residual density grid for each point $[i, j]$ belonging to streamers in the reconstruction space.
13. $P(\theta, \phi, T)$ is added to $\rho(\theta, \phi, T)$ (thus, the residual densities are summed with the current density estimates).
14. $\rho(\theta, \phi, T)$ is smoothed spatially, independently at each time step, with a narrow two-dimensional Gaussian kernel of sigma width [1, 1] bins in longitude, latitude.
15. Any value of $\rho(\theta, \phi, T)$ that is below a minimum threshold is set to that minimum value. This is calculated as the 10th percentile minimum of coronal hole densities.
16. Steps 6−15 are iterated until the difference between the current and previous mean of the absolute residuals, $|P(\theta, \phi, T)|$, becomes small (e.g., 0.0005 for this work). This is a reasonable criterion for termination: if the mean absolute residual does not change much from one iteration to the next, subsequent iterations are redundant.

Appendix B
Convergence of the Method

This appendix shows the convergence of the method for the 2018 November data set. Figure 13(a) shows the observed calibrated brightness used as initial input to the static tomography method, and Figure 13(b) shows the histogram of values within the regions defined as streamers (outlined with the white contour in Figure 13(a)). Figure 13(c) shows the residual gained from subtracting the synthetic static reconstruction brightness from the observed brightness, and Figure 13(d) shows the histogram of this residual. Figures 13(e), (g), and (i) show the residual at iterations 1, 4, and 6, respectively, with Figures 13(f), (h), and (j) showing the histograms. Clearly there is a rapid convergence, particularly at early iterations.

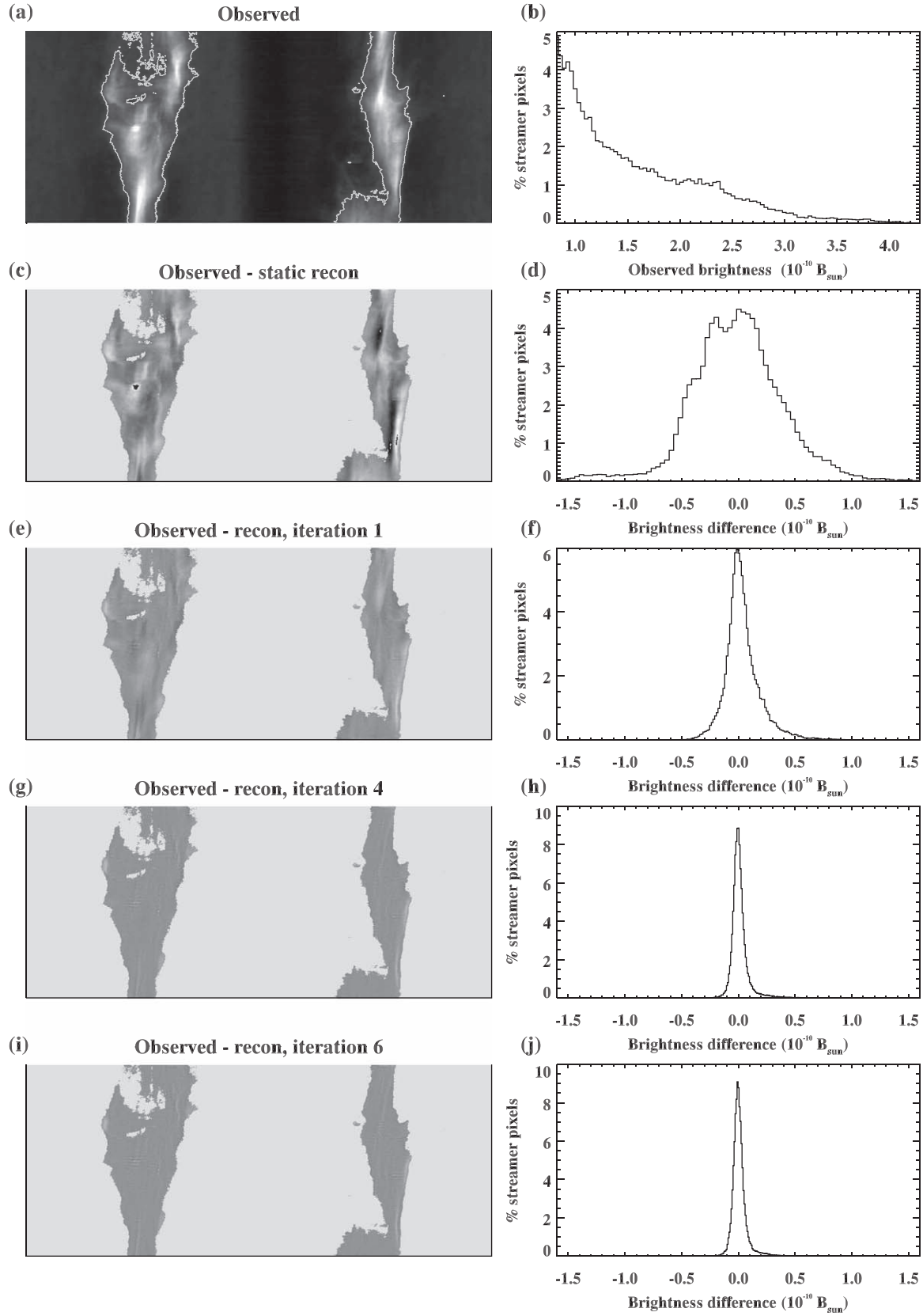

Figure 13. (a) The observed brightness in position angle−time space, with regions defined as streamers highlighted by the white contour (same as Figure 1(a)). (b) Histogram of observed brightness values within streamers, in units of $10^{-10}\,B_{\odot}$, with the y-axis showing the percentage of pixels at each brightness value. (c) The residual between the observed and synthetic brightness for the static reconstruction. Areas outside streamers are colored a uniform light gray. Within the streamers, a value of $-1.6\times10^{-10}\,B_{\odot}$ corresponds to black, and $1.6\times10^{-10}\,B_{\odot}$ to white. (d) Histogram of the values shown in panel (c). (e, g, i) Residuals for iterations 1, 4, and 6, respectively. (f, h, j) Histograms of residuals for iterations 1, 4, and 6, respectively.

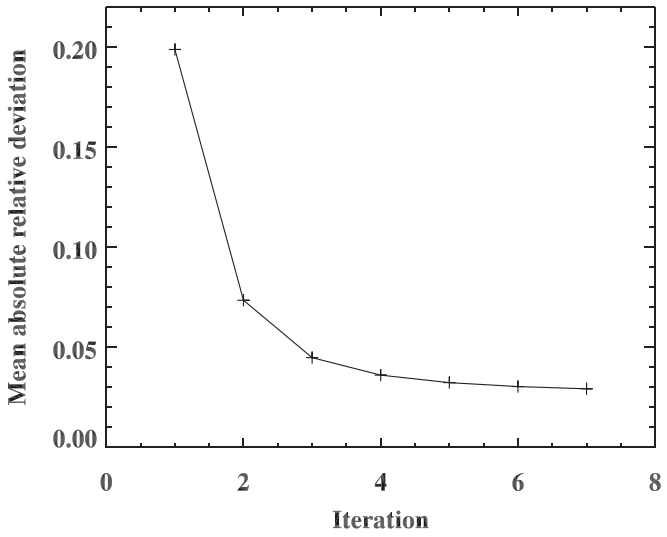

Figure 14. The mean absolute relative deviation (or $\bar{D}$; see Equation (B1)) as a function of iteration number. The first value corresponds to the static reconstruction.

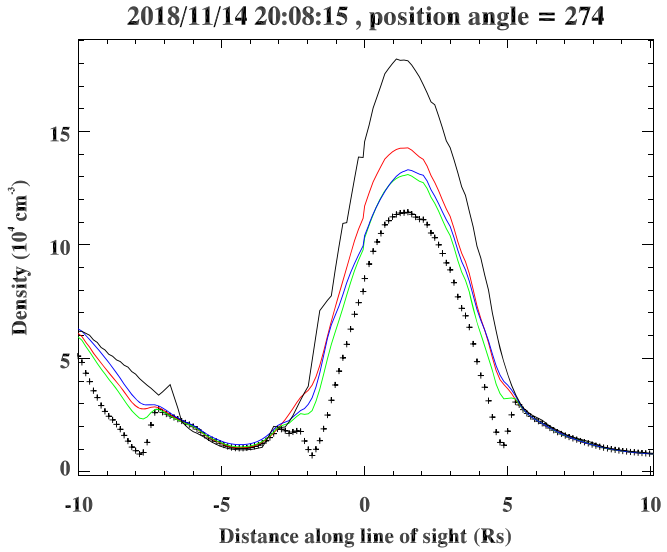

Figure 15. The density along the line of sight of a selected observation point at iteration number 1 (black crosses), 2 (red line), 3 (green line), and 7 (final) iteration (blue line). The selected observation point is for the date and position angle given in the title. For comparison, the density of the static reconstruction is shown as the solid black line.

Figure 14 shows the mean absolute relative deviation, $\bar{D}$, between the observed and reconstructed brightness as a function of iteration number. $\bar{D}$ is defined as

$$\bar{D} = \frac{1}{N}\sum_{i=0}^{N-1}\frac{|B_i - B_i'|}{B_i}, \quad \text{(B1)}$$

where the index i is over the pixels defined as belonging to streamers, and N is the total number of pixels within streamers. As previously, B is the observed brightness and B' is the reconstructed brightness. At the initial iteration, $\bar{D}$ is 0.2. By the second iteration, the additional degree of freedom allowed by time dependence leads to a rapid decrease in $\bar{D}$ to 0.07. At larger iterations, the change in $\bar{D}$ becomes less and converges to a value of approximately 0.03. This limit must include the random noise level in the data, plus any rapid brightness changes possibly present in the data that cannot be resolved by the time-dependent tomography.

Figure 15 shows the density changing with iteration number for a line of sight corresponding to a selected observation point (position angle, time). There are regions along the line of sight where the density remains constant with iteration: these regions are not within streamers, so they remain unchanged other than minor edge differences due to smoothing. At the first iteration, shown by the black crosses, the highest-density streamer has two local minima lobes at the streamer boundary. At the second iteration, the density within the streamer has increased considerably, and the lobes have disappeared. The final density (blue) lies between the initial low and final high densities and is reasonably smooth. For comparison, the solid black line shows the static reconstruction density along this line of sight. Within the main streamer peak, this static density is considerably higher than the time-dependent solutions at all iterations.

ORCID iDs

Huw Morgan https://orcid.org/0000-0002-6547-5838

References

Abbo, L., Ofman, L., Antiochos, S. K., et al. 2016, SSRv, 201, 55
Alzate, N., Habbal, S. R., Druckmüller, M., et al. 2017, ApJ, 848, 84
Alzate, N., Morgan, H., Viall, N., & Vourlidas, A. 2021, ApJ, 919, 98
Badman, S. T., Bale, S. D., Martínez Oliveros, J. C., et al. 2020, ApJS, 246, 23
Bale, S. D., Badman, S. T., Bonnell, J. W., et al. 2019, Natur, 576, 237
Brueckner, G. E., Howard, R. A., Koomen, M. J., et al. 1995, SoPh, 162, 357
Decraemer, B., Zhukov, A. N., & Van Doorsselaere, T. 2019, ApJ, 883, 152
DeForest, C. E., Howard, R. A., Velli, M., et al. 2018, ApJ, 862, 18
DeForest, C. E., Howard, T. A., & McComas, D. J. 2014, ApJ, 787, 124
DeForest, C. E., Matthaeus, W. H., Viall, N. M., et al. 2016, ApJ, 828, 66
Domingo, V., Fleck, B., & Poland, A. I. 1995, SoPh, 162, 1
Druckmüller, M., Habbal, S. R., & Morgan, H. 2014, ApJ, 785, 14
Gibson, S. E., Fludra, A., Bagenal, F., et al. 1999, JGR, 104, 9691
Habbal, S. R., Morgan, H., & Druckmüller, M. 2014, ApJ, 793, 119
Hayes, A. P., Vourlidas, A., & Howard, R. A. 2001, ApJ, 548, 1081
Howard, R. A., Moses, J. D., Socker, D. G., Dere, K. P., & Cook, J. W. 2002, AdSpR, 29, 2017
Kaiser, M. L. 2005, AdSpR, 36, 1483
Morgan, H. 2011a, ApJ, 738, 189
Morgan, H. 2011b, ApJ, 738, 190
Morgan, H. 2013, MNRAS, 433, L74
Morgan, H. 2015, ApJS, 219, 23
Morgan, H. 2019, ApJS, 242, 3
Morgan, H., & Cook, A. C. 2020, ApJ, 893, 57
Morgan, H., & Habbal, S. R. 2007a, A&A, 464, 357
Morgan, H., & Habbal, S. R. 2007b, A&A, 465, L47
Morgan, H., & Habbal, S. R. 2007c, A&A, 471, L47
Morgan, H., & Habbal, S. R. 2010, ApJ, 710, 1
Morgan, H., Jeska, L., & Leonard, D. 2013, ApJS, 206, 19
Morgan, H., & Taroyan, Y. 2017, SciA, 3, e1602056
Quémerais, E., & Lamy, P. 2002, A&A, 393, 295
Sheeley, N. R., & Wang, Y.-M. 2001, ApJL, 562, L107
Sheeley, N. R., Wang, Y.-M., Hawley, S. H., et al. 1997, ApJ, 484, 472
Strachan, L., Suleiman, R., Panasyuk, A. V., Biesecker, D. A., & Kohl, J. L. 2002, ApJ, 571, 1008
Thernisien, A. F., & Howard, R. A. 2006, ApJ, 642, 523
Viall, N. M., Spence, H. E., Vourlidas, A., et al. 2010, SoPh, 267, 175
Viall, N. M., & Vourlidas, A. 2015, ApJ, 807, 176
Vibert, D., Peillon, C., Lamy, P., Frazin, R. A., & Wojak, J. 2016, A&C, 17, 144
Wang, Y.-M., Sheeley, N. R., Howard, R. A., et al. 1999, GeoRL, 26, 1203